

TiO₂/g-C₃N₄ nanosheets hybrid photocatalyst with enhanced photocatalytic activity under visible light irradiation

Yongmei Wu^{1,2} · Li Tao² · Jie Zhao¹ · Xiu Yue¹ ·
Wenye Deng¹ · Yingxuan Li¹ · Chuanyi Wang¹

Received: 28 July 2015 / Accepted: 17 August 2015 / Published online: 23 August 2015
© Springer Science+Business Media Dordrecht 2015

Abstract The nanosheets TiO₂/g-C₃N₄ hybrid material with efficient visible-light photocatalytic activity was prepared by a facile solvothermal method. The as-prepared TiO₂/g-C₃N₄ nanosheets composite was thoroughly characterized by X-ray diffraction, Fourier transform infrared spectroscopy, transmission electron microscopy, N₂ adsorption–desorption analysis, UV–Vis diffuse reflectance spectroscopy, and X-ray photoelectron spectroscopy. As evaluated by the degradation of methylene blue under visible light irradiation, TiO₂/g-C₃N₄ hybrid composites exhibit much higher photocatalytic activity than pristine g-C₃N₄ and TiO₂, respectively. The significant enhancement in photodegradation activity over the TiO₂/g-C₃N₄ photocatalyst can be ascribed to the combined effects of the nanosheet structure and subsequent efficient separation of photogenerated charge carriers. A tentative mechanism for the photodegradation process was proposed.

Keywords TiO₂ · Graphitic carbon nitride · Hybrid composites · Nanosheets · Photocatalyst

✉ Yongmei Wu
wuyongmeismx@163.com

✉ Chuanyi Wang
cywang@ms.xjb.ac.cn

¹ Laboratory of Environmental Sciences and Technology, Xinjiang Technical Institute of Physics & Chemistry, Key Laboratory of Functional Materials and Devices for Special Environments, Chinese Academy of Science, 40-1 South Beijing Road, Ürümqi 830011, Xinjiang, People's Republic of China

² Department of Chemical and Environmental Engineering, Xinjiang Institute of Engineering, Ürümqi 830091, People's Republic of China

Introduction

Recently, the related fully condensed polymers known as graphitic carbon nitride ($g\text{-C}_3\text{N}_4$) has attracted considerable attention. Graphitic carbon nitride is the most stable allotrope, with a layered structure similar to graphene and has metal-free chemical compositions of C, N, and H [1]. Meanwhile, a narrow band gap semiconductor ($E_g = 2.7$ eV) in $g\text{-C}_3\text{N}_4$ is of growing interest as a photocatalyst and has been extensively studied in visible light-driven water splitting and degradation of organic pollutants [2–4]. However, the photocatalytic efficiency of single $g\text{-C}_3\text{N}_4$ is limited due to the high recombination probability of photogenerated electron–hole pairs [5, 6]. In order to improve photocatalytic activity, several efforts have been developed to improve the photocatalytic performance of $g\text{-C}_3\text{N}_4$ in terms of introducing heteroatoms [7–10], sensitized by dyes [11], coupled with semiconductors or polymers [12–16], and controlling morphology [17–19]. Nevertheless, a simple development of highly efficient $g\text{-C}_3\text{N}_4$ remains a significant challenge.

To date, the combination of $g\text{-C}_3\text{N}_4$ and TiO_2 into a heterostructure presents a feasible and inspiring route towards improved charge separation in the electron transfer process [20–25]. Yu et al. [26] synthesized $g\text{-C}_3\text{N}_4\text{-TiO}_2$ nanocomposites by a facile calcination route using P25 and urea, resulting in higher photoactivity for the decomposition of HCHO than that of single-phase C_3N_4 and bare TiO_2 . The $g\text{-C}_3\text{N}_4/\text{TiO}_2$ photocatalyst with extremely simple steps using cyanamide and anatase TiO_2 as resources was reported by Lei et al. [27]. This photocatalyst shows prominent improvement in degradation of Acid Orange 7 dyes under both visible and UV light [27]. Colón et al. [28] reported the preparation of $g\text{-C}_3\text{N}_4\text{-TiO}_2$ composites with different $g\text{-C}_3\text{N}_4$ loadings by simple impregnation, giving good photoactivity for the degradation of phenol under UV irradiation. Zhang et al. [29] has found that well-dispersed TiO_2 nanocrystals with (001) facets prepared in situ on $g\text{-C}_3\text{N}_4$ through a facile solvothermal method exhibit higher efficiency for photocatalytic degradation of phenol as compared to pure $g\text{-C}_3\text{N}_4$ and TiO_2 or mechanically mixed $\text{TiO}_2/g\text{-C}_3\text{N}_4$. Therefore, combining TiO_2 with $g\text{-C}_3\text{N}_4$ to form composite photocatalysts seems to be an effective approach to construct a heterojunction structure leading to enhanced photoactivity. In this work, TiO_2 hybridized with $g\text{-C}_3\text{N}_4$ nanosheets were prepared by a facile approach. The TiO_2 nanosheets prepared by solvothermal reaction were found to be well anchored on the surface of $g\text{-C}_3\text{N}_4$ nanosheets, endowing the hybrid with an interfacial junction. The as-prepared $\text{TiO}_2/g\text{-C}_3\text{N}_4$ nanosheets composites have shown stronger photocatalytic performance than pure TiO_2 nanosheets and $g\text{-C}_3\text{N}_4$.

Experimental sections

Catalyst preparation

The polymeric $g\text{-C}_3\text{N}_4$ was synthesized by calcination with melon as precursor. Typically, 12 g of melon was put into a crucible with a cover and then heated at

550 °C in a muffle furnace for 4 h with a heating rate of 10 °C min⁻¹. The resultant yellow powder was washed with 1.0 M HCl and distilled water and then sonicated in methanol for 60 min, dried at 100 °C, and collected for further use.

A 1.5 g amount of urea was dissolved in 10 mL of anhydrous ethanol, then 1.0 mL distilled water was added slowly with stirring for 30 min at room temperature (solution A). A certain amount of tetrabutyl titanate (TBT) was dissolved into 10 mL anhydrous ethanol (solution B). After that, solution A was added drop-wise to solution B under magnetic stirring. The resultant mixture was stirred at room temperature for 2 h until the transparent sol was obtained. One gram of g-C₃N₄ was added into the transparent sol, and the mixture was sonicated for 60 min to disperse completely g-C₃N₄. Subsequently, the mixture was transferred into a 50 mL Teflon-inner-liner stainless steel autoclave. The autoclave was kept at 150 °C for 16 h. Finally, the precipitate gained was washed with distilled water and dried at 100 °C for 24 h. The weight percentages of TiO₂ to g-C₃N₄ were varied by varying the weight of TiO₂, and the samples were presented as x % TiO₂/g-C₃N₄, where x is the weight content of TiO₂. For comparison, pure TiO₂ was also prepared by the same procedure without adding g-C₃N₄, which is denoted as TiO₂.

Catalyst characterization

The crystal structures of samples were determined by an X-ray diffractometer (a Bruker D8) with Cu K α radiation ($\lambda = 0.15418$ nm). Thermogravimetric analysis was conducted on an NETZSCH STA 449F3 instrument. The experiment temperature ranged from 25 to 1000 °C at a constant heating rate of 10 °C/min in air. Optical properties were analyzed with a spectrophotometer (Shimadzu SolidSpec-3700DUV) and converted from reflection to absorbance by the standard Kubelka–Munk method. FT-IR measurements were performed using a Fourier transform infrared (FT-IR) spectrometer (Nicolet 670) only in the mid-infrared range of the instrument (400–4000 cm⁻¹) for samples dispersed in KBr pellets in 1:99. X-ray photoelectron spectroscopy (XPS) was recorded with a Perkin Elmer PHI 5000C ESCA System with Al K α radiation operated at 250 W. The shift of binding energy due to relative surface charging was corrected using the C 1s level at 284.6 eV as an internal standard. The nitrogen adsorption–desorption isotherms at 77 K were investigated using a nitrogen adsorption apparatus (QUADRASORB IQ, Quantachrome Instrument Corp). The morphology was observed using a scanning electron microscope (SEM, JSM5600LV, JEOL Ltd.) and JEM-100CX Transmission Electron Microscopy (TEM, JEOL, Japan). The photoelectrochemical measurements were carried out on a Shanghai Chenhua CHI-660D electrochemical system, using a conventional three-electrode cell. The counter and the reference electrodes were Pt wire and saturated calomel electrodes (SCE), respectively. The electrolyte solution was 0.5 M Na₂SO₄. The working electrodes were prepared as follows: 0.1 g of catalyst sample was mixed with 0.02 g PEG, and 0.5 mL distilled water was added to make slurry. The slurry was then injected onto a 1.0 cm \times 1.0 cm ITO glass electrode, and these electrolytes were dried at 60 °C for 2 h and then calcined at 250 °C for 4 h.

Photocatalytic activity test

The photocatalytic activities of the samples were measured by the degradation of aqueous methylene blue under visible light. About 100 mg of a sample photocatalyst was first added to an aqueous solution of methylene blue (100 mL, $20 \text{ mg}\cdot\text{L}^{-1}$) in a beaker. The pH value of mixture was kept at 7.0. The solution was sonicated for 10 min and stirred for 1 h in the dark to reach the adsorption–desorption equilibrium. This is followed by irradiation of visible light obtained from 400 W Xe lamp with a cutoff filter ($\lambda > 420 \text{ nm}$), and the average visible light intensity was $30 \text{ mW}\cdot\text{cm}^{-2}$. At certain time intervals, 3 mL aliquots were sampled and centrifuged to remove the photocatalyst particles. Then the filtrates were analyzed by recording variations in the absorption band maximum (663 nm) in the UV–Vis spectra of MB. The reproducibility was checked by repeating the measurements at least three times and was found to be within the acceptable limit ($\pm 5 \%$).

Results and discussion

XRD analysis

Figure 1 shows the powder XRD patterns of C_3N_4 , TiO_2 , and $\text{TiO}_2/\text{g-C}_3\text{N}_4$ composite. Two pronounced peaks were found in $\text{g-C}_3\text{N}_4$ at 27.4° and 13.1° , which can be indexed to (002) and (001) diffraction planes of the graphite-like carbon nitride [5, 21] and correspond to the characteristic interplanar staking peak of aromatic systems and the inter-layer structural packing, respectively. For TiO_2

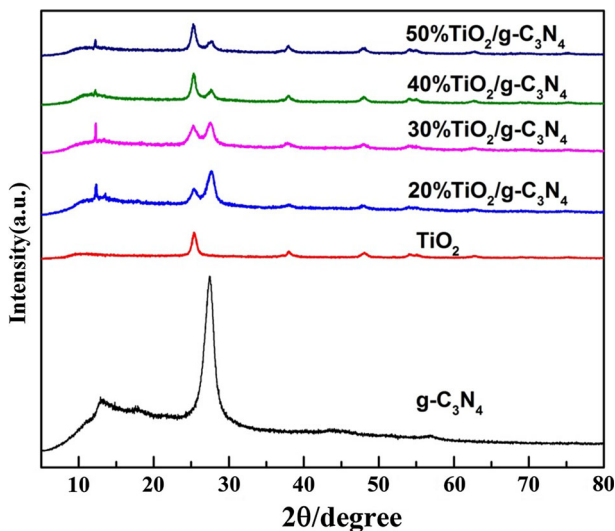


Fig. 1 XRD patterns of the samples

sample, its diffraction peaks are in good agreement with the anatase phase of TiO₂ (JCPDS no. 21-1272, space group: I4₁/amd (141)) [30–32]. The TiO₂/g-C₃N₄ composite presents a two-phase composition: g-C₃N₄ and TiO₂, indicating that the hybridization of TiO₂ with g-C₃N₄ did not change its structure. Additionally, it showed that the intensity of diffraction peaks of g-C₃N₄ decrease with the increasing of loading of TiO₂.

FT-IR analysis

Figure 2 shows the Fourier transform infrared (FT-IR) spectra of C₃N₄, TiO₂ and TiO₂/g-C₃N₄ composite, respectively. In the spectrum of g-C₃N₄, the absorption band near 1640 cm⁻¹ is attributed to C–N stretching, and the three at 1240, 1320, and 1403 cm⁻¹ to aromatic C–N stretching [33, 34]. The band near 807 cm⁻¹ corresponds to the out-of-plane bending vibration of the triazine units [2, 35]. A broad band near 3140 cm⁻¹ corresponds to the stretching modes of terminal NH₂ or NH groups at the defect sites of the aromatic ring [36]. As to the spectrum of pure TiO₂, the weak absorption band centered at 443 cm⁻¹ is attributed to the Ti–O–Ti stretching vibration [37]. As expected, all the TiO₂/g-C₃N₄ samples show typical peaks of both compounds, confirming a successful combination of g-C₃N₄ and TiO₂.

Microstructure analysis

Figure 3 shows the SEM images of TiO₂, g-C₃N₄ and TiO₂/g-C₃N₄ composites. From Fig. 3a, it can be seen that the obvious agglomeration of nanoparticles of TiO₂. Also, the g-C₃N₄ sample shows obvious two-dimensional lamellar structures with wrinkle and irregular folding structures (seen from Fig. 3b). The images of

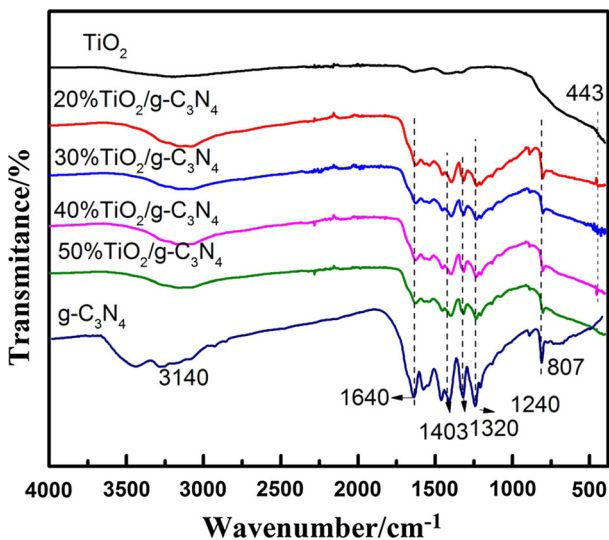


Fig. 2 FT-IR spectra of the samples

20 %TiO₂/g-C₃N₄ and 40 %TiO₂/g-C₃N₄ in Fig. 3c, d resemble a quite distinct morphology from TiO₂ combined with layer-like texture of g-C₃N₄. This indicates that TiO₂ was successfully deposited on the surface of g-C₃N₄. To confirm further the chemical composition of the as-prepared samples, the EDS map of 40 %TiO₂/g-

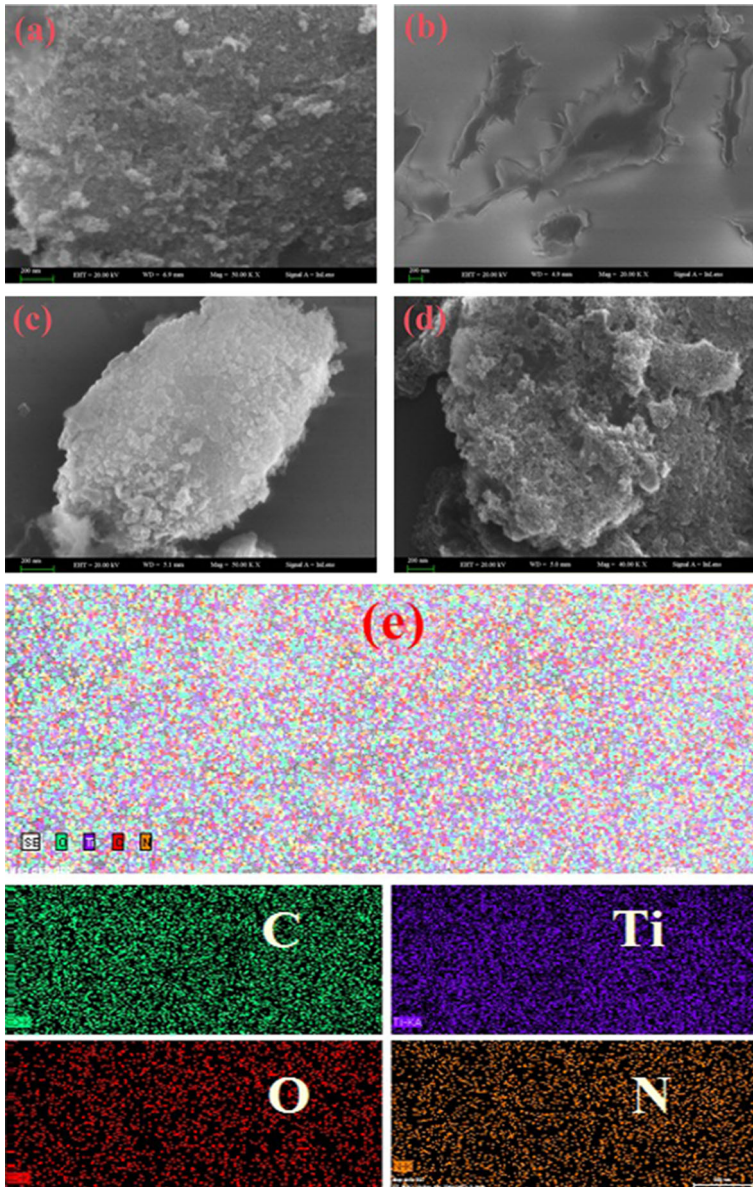


Fig. 3 SEM images of **a** TiO₂, **b** g-C₃N₄, **c** 20 %TiO₂/g-C₃N₄, **d** 40 %TiO₂/g-C₃N₄, **e** EDS map of 40 %TiO₂/g-C₃N₄

C₃N₄ was taken as shown in Fig. 3e. As can be obviously observed, C, N, O, and Ti elements is found, which verifies that the sample is composed of the four elements above.

The TEM images of g-C₃N₄, TiO₂ and 40 %TiO₂/g-C₃N₄ are shown in Fig. 4. As shown in Fig. 4a, tremella-like g-C₃N₄ is composed of a number of micro-scale layers, coinciding with the SEM observation. From Fig. 4b, TiO₂ is composed of a lot of thinner nanosheets. It was reported that TiO₂ with nanosheets structure could be synthesized by the solvothermal method when tetrabutyl titanate (TBT) is mixed with ethanol in the presence of acid [38]. Our results were similar to the literature reported [38]. For 40 %TiO₂/g-C₃N₄ sample (Fig. 4c), TiO₂ nanosheets were combined with g-C₃N₄ nanosheets. It can be observed from Fig. 4d that clear lattice fringes for the identification of crystallographic spacing, and the fringe spacing of ca. 0.35 nm matches well with the anatase TiO₂ (101) plane. During solvothermal treatment, the nanosheet TiO₂ assembled on the surface of g-C₃N₄ nanosheet to achieve a minimum surface energy [39]. This type of interfacial contact would facilitate the transfer of photo-generated charge carriers between g-C₃N₄ and TiO₂ when used as a heterogeneous photocatalyst.

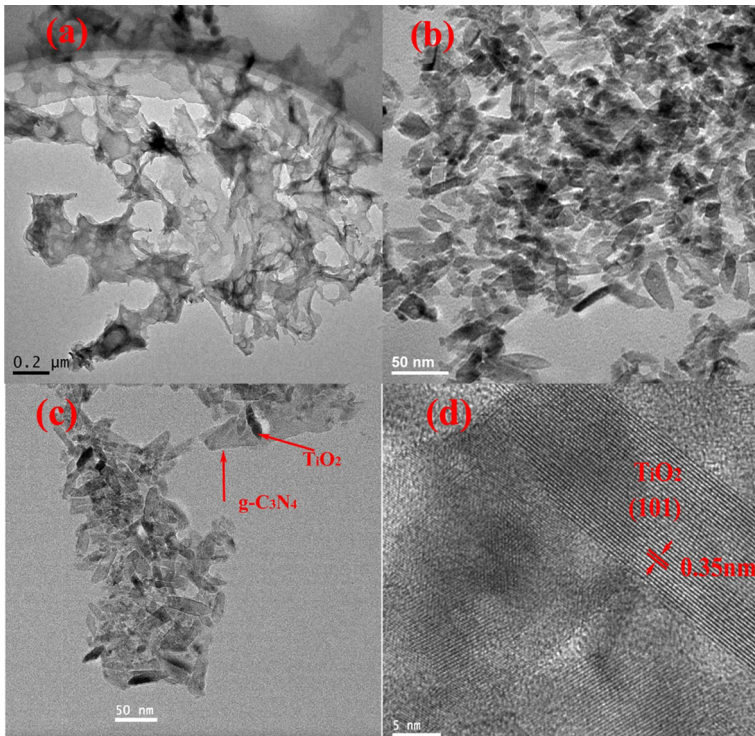


Fig. 4 TEM images of **a** g-C₃N₄, **b** TiO₂, **c** 40 %TiO₂/g-C₃N₄, **d** HRTEM of 40 %TiO₂/g-C₃N₄

TG-DSC and BET analysis

To understand the TiO_2 contents in the final products, thermogravimetric analysis was performed from room temperature to $1000\text{ }^\circ\text{C}$ at a heating rate of $10\text{ }^\circ\text{C min}^{-1}$ under air conditions. As shown in Fig. 5a and b, in the case of $\text{g-C}_3\text{N}_4$, a rapid weight loss region occurring from about $680\text{ }^\circ\text{C}$ is observed, which can be assigned to the combustion of $\text{g-C}_3\text{N}_4$. It was reported that the tri-s-triazine ring structure and the high temperature condensation make $\text{g-C}_3\text{N}_4$ have a high thermal stability up to $600\text{ }^\circ\text{C}$ [35]. The weight of the 20 % $\text{TiO}_2/\text{g-C}_3\text{N}_4$ sample decreases rapidly in the temperature range $450\text{--}600\text{ }^\circ\text{C}$, indicating that the combustion of $\text{g-C}_3\text{N}_4$ occurred in this temperature range. However, it can be seen that a rapid weight loss temperature occurs at $564\text{ }^\circ\text{C}$, which is lower than single $\text{g-C}_3\text{N}_4$. This indicates the easy combustion of $\text{g-C}_3\text{N}_4$ when TiO_2 deposited on the surface of $\text{g-C}_3\text{N}_4$. The contents of TiO_2 in the composites of $\text{TiO}_2/\text{g-C}_3\text{N}_4$ could be easily derived from the weight remainder after heating the samples over $1000\text{ }^\circ\text{C}$. TiO_2 contents in 20 % $\text{TiO}_2/\text{g-C}_3\text{N}_4$ sample were determined to be 14.35 %. TiO_2 contents in other $\text{TiO}_2/\text{g-C}_3\text{N}_4$ samples are listed in Table 1.

Figure 6 shows the nitrogen adsorption–desorption isotherms for 40 % $\text{TiO}_2/\text{g-C}_3\text{N}_4$ at 77 K. The 40 % $\text{TiO}_2/\text{g-C}_3\text{N}_4$ sample yields type IV isotherms, and an H3-type hysteresis loop, indicating the presence of slit-like pores and the formation of large mesopores and macropores [26, 40]. The pore distributions (inset in Fig. 6) are very broad, further indicating the existence of mesopores and macropores. The BET surface areas of $\text{TiO}_2/\text{g-C}_3\text{N}_4$ with different loading of TiO_2 are listed in Table 1. It is found that pure TiO_2 ($144\text{ m}^2/\text{g}$) has a larger surface area than that of $\text{g-C}_3\text{N}_4$ ($26.3\text{ m}^2/\text{g}$). When $\text{g-C}_3\text{N}_4$ nanosheets are facet coupled with TiO_2 nanosheets, the surface areas of $\text{TiO}_2/\text{g-C}_3\text{N}_4$ hybrids are increased with the increased content of TiO_2 .

UV–Vis DRS

The optical absorption properties of $\text{g-C}_3\text{N}_4$, TiO_2 , and $\text{TiO}_2/\text{g-C}_3\text{N}_4$ hybrids with different TiO_2 loading are investigated by UV–Vis DRS spectra in Fig. 7. The absorption onset of $\text{g-C}_3\text{N}_4$ is found at about 460 nm , corresponding to band gap

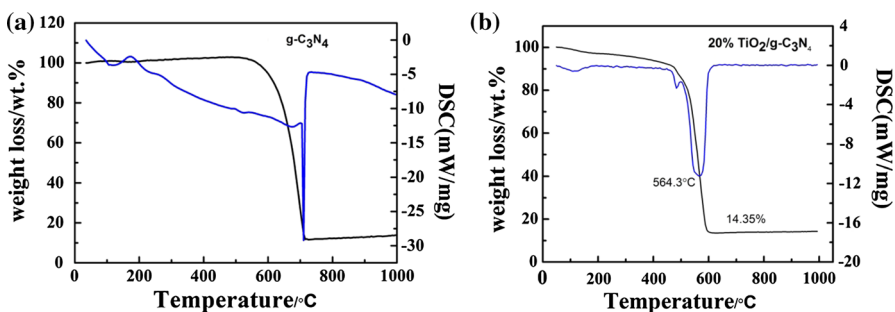
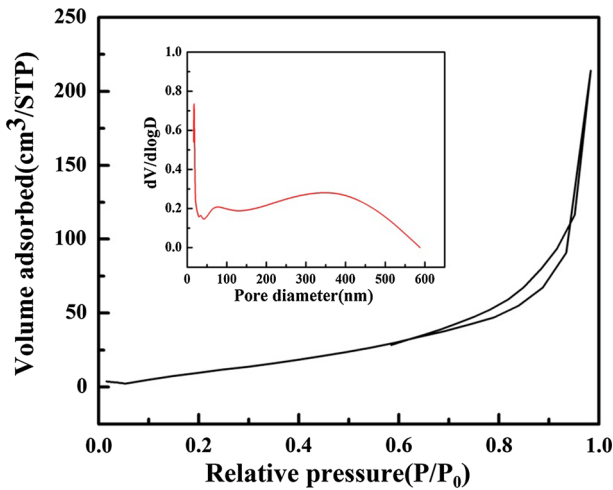
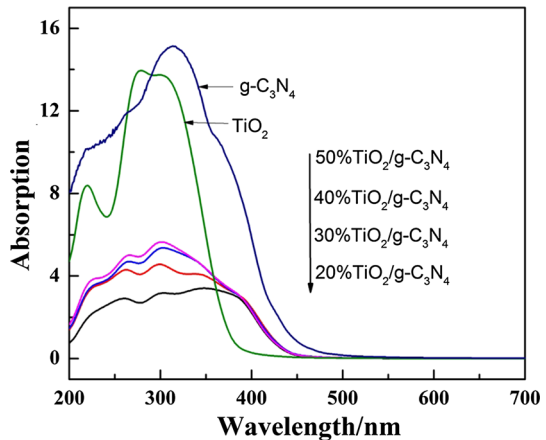


Fig. 5 TG-DSC curves of **a** $\text{g-C}_3\text{N}_4$; **b** 20 % $\text{TiO}_2/\text{g-C}_3\text{N}_4$

Table 1 TiO₂ content and BET surface areas of the samples

Sample	TiO ₂ (wt%)	S _{BET} (m ² /g)
TiO ₂	100	144
g-C ₃ N ₄	0	20.9
20 %TiO ₂ /g-C ₃ N ₄	14.53	56.3
30 %TiO ₂ /g-C ₃ N ₄	31.72	70.3
40 %TiO ₂ /g-C ₃ N ₄	44.87	77.0
50 %TiO ₂ /g-C ₃ N ₄	55.41	87.4

**Fig. 6** N₂ adsorption-desorption isotherm of 40 %TiO₂/g-C₃N₄ and corresponding Barrett-Joyner-Halenda (BJH) pore-size distribution plots (*inset*)**Fig. 7** UV-Vis absorption spectra of the samples

energy of 2.7 eV. This result is consistent with other groups' work [12, 41]. Meanwhile, the band gap of TiO_2 is estimated to be about 3.2 eV with the absorption edge of 384 nm from its UV-Vis DRS spectrum in Fig. 7. After hybridization with TiO_2 , the absorbance of $\text{TiO}_2/\text{g-C}_3\text{N}_4$ is extended to the visible region due to the presence of $\text{g-C}_3\text{N}_4$. The absorption edge of the hybrid are at 450 nm corresponding to band gap energy of 2.8 eV. It was also seen that the absorbance onset of the hybrid materials are unchanged; however, the absorption intensity of UV region increase with the loading amount of TiO_2 increasing.

XPS analysis

XPS analysis was carried out to analyze further the surface chemical composition of the as-prepared samples and to identify the chemical status of the Ti, C, O, and N elements in the samples. Figure 8a illustrates XPS survey spectra of $\text{g-C}_3\text{N}_4$, TiO_2 , and 40 % $\text{TiO}_2/\text{g-C}_3\text{N}_4$ samples and elements of C, N, O, Ti were detected. As seen in Fig. 8b, a signal deconvolution after Gaussian curve fitting three peaks centered at 284.6, 285.1, 287.5 eV can be observed for C 1s of $\text{g-C}_3\text{N}_4$. The peak located at 284.6 eV can be assigned to the C-C or adventitious carbon. The peak at 287.5 eV can be ascribed to the N-C=N group of $\text{g-C}_3\text{N}_4$ and the peak at 285.7 eV can be

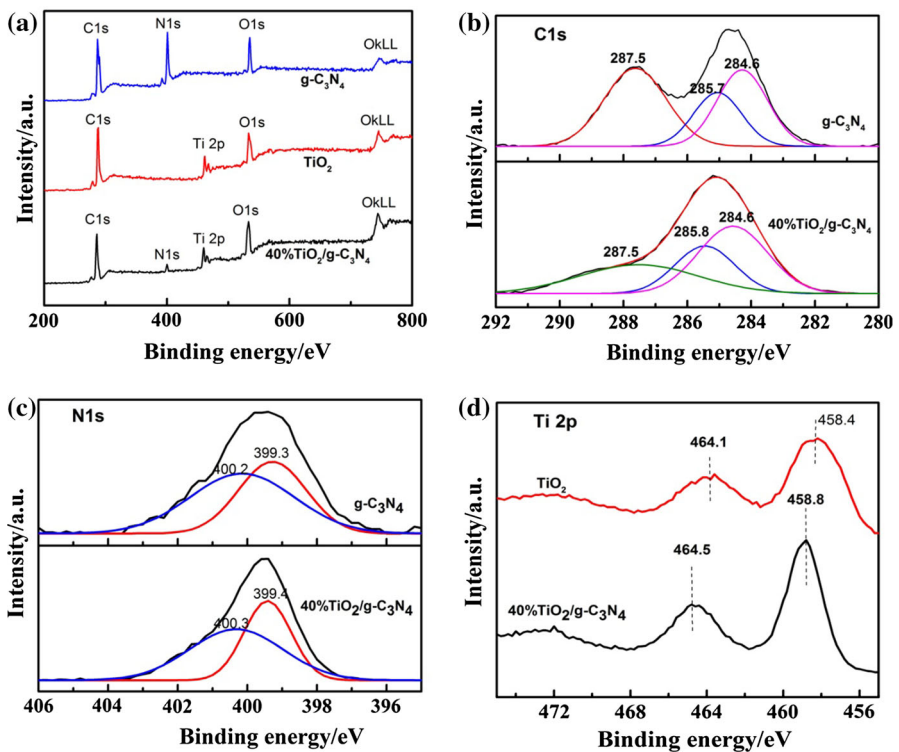


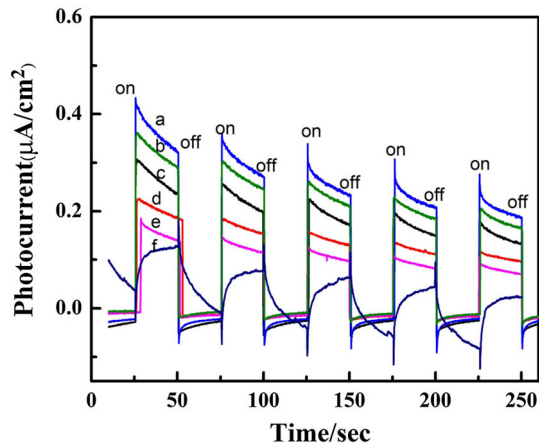
Fig. 8 XPS spectra of TiO_2 , $\text{g-C}_3\text{N}_4$, TiO_2 and 40 % $\text{TiO}_2/\text{g-C}_3\text{N}_4$ samples

attributed to C–O species from incompletely reacted oxygen-containing intermediates formed in the heating process [5, 12, 26]. For the 40 %TiO₂/g-C₃N₄ sample, in comparison with that of pure g-C₃N₄, the peak at 285.7 eV is attributed to C–O species positive shift to 285.8 eV. This can be ascribed to the hybridization of TiO₂ and g-C₃N₄. Figure 8c shows the N 1s spectrum of g-C₃N₄ and 40 %TiO₂/g-C₃N₄ sample. The N 1s peak of g-C₃N₄ can be deconvoluted into two fitted peaks at 399.3 and 400.2 eV. The two peaks found can be ascribed to the sp²-hybridized nitrogen (C=N–C) at 399.3 eV and tertiary nitrogen (N–C₃) at 400.2 eV, respectively [42]. The average C/N ratio calculated in our case is 0.72, in accordance with values reported for g-C₃N₄ obtained this way [2]. Figure 8d displays the XPS Ti 2p spectra of TiO₂ and 40 %TiO₂/g-C₃N₄ samples. For TiO₂ sample, two peaks for the Ti 2p spectra were observed at 458.4 eV and 464.1 eV, assigned to Ti 2p_{3/2} and Ti 2p_{1/2}, in good agreement with the presence of Ti(IV) [43]. With respect to the 40 %TiO₂/g-C₃N₄ sample, the binding energy of Ti 2p_{3/2} and 2p_{1/2} is located at around 458.8 eV and 464.6 eV, respectively, positively shifted by 0.4 eV, suggesting the possible interaction between g-C₃N₄ and TiO₂.

Photocurrent measurements

The photocurrent is widely regarded as the most efficient evidence for demonstrating the separation of electrons and holes in the composite photocatalysts [44, 45]. The relationship is commonly recognized as the higher the photocurrent, the higher the electron–hole separation efficiency, and thus the higher the photocatalytic activity. Figure 9 shows the photocurrent–time curves of TiO₂, g-C₃N₄, and the TiO₂/g-C₃N₄ hybrid materials with five on–off intermittent irradiation cycles. The 40 %TiO₂/g-C₃N₄ sample presents higher photocurrent intensity, thus it can have a lower rate of electrons and holes recombination.

Fig. 9 Photoelectric conversion performances of samples in 0.5 M Na₂SO₄ aqueous solutions. *a* 40 %TiO₂/g-C₃N₄, *b* 50 %TiO₂/g-C₃N₄, *c* 30 %TiO₂/g-C₃N₄, *d* 20 %TiO₂/g-C₃N₄, *e* TiO₂, *f* g-C₃N₄



Photocatalytic activity

The photoinduced degradation of MB is carried out under visible light illumination in aqueous $\text{TiO}_2/\text{g-C}_3\text{N}_4$ suspensions. Figure 10 displays the changes of the MB concentration versus the reaction time over the $\text{TiO}_2/\text{g-C}_3\text{N}_4$ catalysts and the corresponding first-order kinetics plot by the equation of $\ln(C_0/C) = k^{-1}t$, where C_0 and C are the MB concentrations in solution at times 0 and t , respectively, and k^{-1} is the apparent first-order rate constant. As it can be observed in Fig. 10a, TiO_2 presents a rather low degradation rate, which can be attributed to the self-sensitization of MB. At the same time, $\text{g-C}_3\text{N}_4$ also shows lower MB degradation after 3 h of reaction. Although $\text{g-C}_3\text{N}_4$ sample shows strong absorption of visible light, its low degradation efficiency may be due to the poor surface areas. However, the incorporation of different amounts of TiO_2 clearly enhances the photocatalytic activity of $\text{g-C}_3\text{N}_4$ (Fig. 9b). It is easy to find that the photocatalytic activity increases with the amount of TiO_2 increasing. The 40 % $\text{TiO}_2/\text{g-C}_3\text{N}_4$ sample exhibits a maximum value; the degradation rate constant k^{-1} is 0.014 min^{-1} which is above 7 times as high as that of TiO_2 (0.002 min^{-1}) and 10 times than that of $\text{g-C}_3\text{N}_4$ (0.0012 min^{-1}).

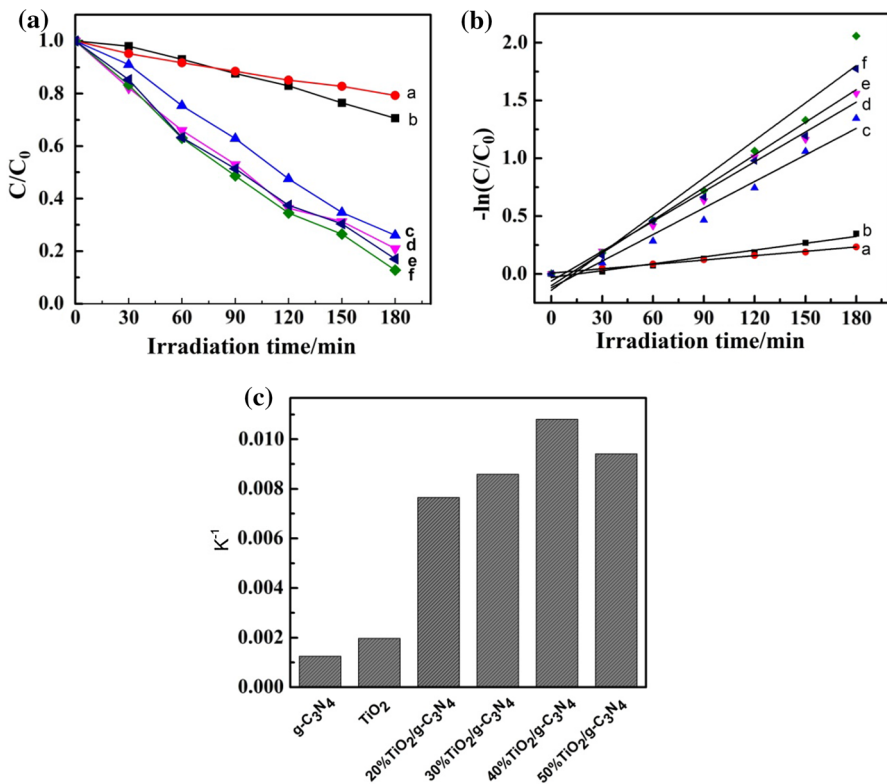


Fig. 10 Photocatalytic activity of the samples for degradation of 20 mg/L MB under visible light irradiation (a); the corresponding first-order kinetics plot (b), (c) apparent rate constant K^{-1} of samples. a TiO_2 , b $\text{g-C}_3\text{N}_4$, c 20 % $\text{TiO}_2/\text{g-C}_3\text{N}_4$, d 30 % $\text{TiO}_2/\text{g-C}_3\text{N}_4$, e 50 % $\text{TiO}_2/\text{g-C}_3\text{N}_4$, f 40 % $\text{TiO}_2/\text{g-C}_3\text{N}_4$

The as-prepared nanosheet 40 %TiO₂/g-C₃N₄ hybrid photocatalyst showed excellent photocatalytic performance on the degradation of MB under visible light irradiation. Based on the characterization of structure and properties, the efficient photocatalytic activity should be mainly ascribed to the following reasons. Firstly, the structure characterizations have proven that the TiO₂/g-C₃N₄ photocatalyst is a two-phase composite. Considering that the composite presents much higher photocatalytic activity than the component phase alone, it is reasonable that there might have synergetic effect between TiO₂ and g-C₃N₄. To evaluate further the synergetic effect on the photocatalytic activity of the g-C₃N₄ and TiO₂, g-C₃N₄ (0.0056 g) and TiO₂ (0.044 g) were mechanically mixed with respect to the degradation of MB under visible light irradiation. The mechanically mixed sample degraded 23 % of the MB for 180 min of visible light irradiation. Its photocatalytic activity is much lower than that of the heterostructure sample 40 %TiO₂/g-C₃N₄. This result suggests that the heterostructure between TiO₂ and g-C₃N₄ plays a major role in the enhancement of photocatalytic activity. Actually, many researchers have attributed the effect to the efficient charge transfer at the interface of two semiconductors, which would result in an effective photoexcited electron–hole separation and, consequently, enhance the photocatalytic activity [26, 27]. The scheme (Fig. 11) for electron–hole separation and transport at the light-driven heterostructure TiO₂/g-C₃N₄ photocatalyst as well as the MB degradation mechanism are discussed as follows. According to the relative research, the valence band (VB) potentials and the conduction band (CB) edge potentials of a semiconductor at the point of zero charge can be theoretically predicted [45]:

$$E_{VB} = X - E_c + 0.5E_g \quad (1)$$

$$E_{CB} = E_{VB} - E_g \quad (2)$$

where X represents the electronegativity of the semiconductor, which is the geometric mean of the electronegativity of the constituent atoms, the X values for the

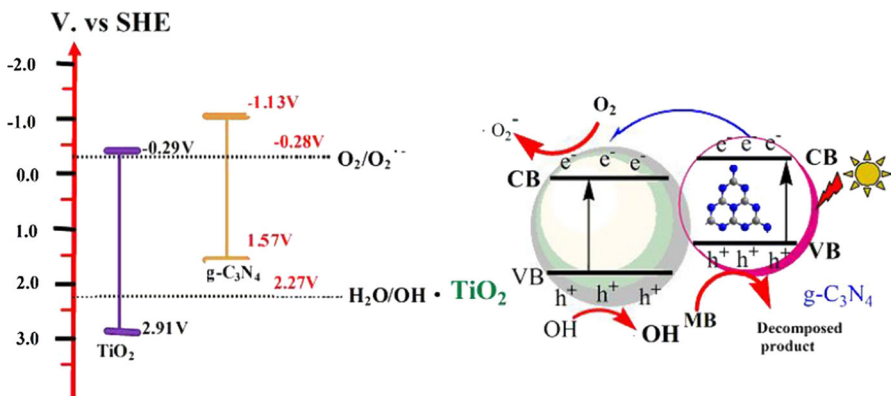


Fig. 11 Schematic illustration for the mechanism of photo-induced charge carrier transfers in TiO₂/g-C₃N₄ nanosheets under visible light irradiation,

g-C₃N₄ and TiO₂ materials are 4.72 eV and 5.81 eV; E_c is the energy of free electrons on the hydrogen scale (here about 4.5 eV), E_g is the band gap energy of the semiconductor. According to our results of UV–Vis DRS, the E_g of g-C₃N₄ and TiO₂ were estimated at 2.70 eV and 3.20 eV, respectively. Therefore, the CB and VB edge potentials of g-C₃N₄ were determined at −1.13 eV and +1.57 eV, respectively. The CB and VB edge potentials of TiO₂ were calculated at −0.29 eV and +2.91 eV, respectively. As shown in Fig. 11.

Under visible light irradiation, g-C₃N₄ absorbed visible light and excited. The photogenerated electrons first transferred from valence band of g-C₃N₄ to conduction band. Since the CB edge potential of g-C₃N₄ (−1.13 eV) was more negative than that of TiO₂ (−0.29 eV), the photoinduced electrons on g-C₃N₄ particle surfaces transferred easily to TiO₂. Then, the electrons stored in the CB of TiO₂ are trapped by O₂ near the surface of TiO₂ to form superoxide radicals $\cdot\text{O}_2^-$ produces HOO \cdot radicals, which can transform into H₂O₂ by further trapping electrons, and finally into $\cdot\text{OH}$ radicals for the further photocatalytic degradation of MB [46]. Meanwhile, the photogenerated holes in TiO₂, which have a high oxidation potential (+2.91 V vs. SHE), diffuse to the surfaces, and they directly degrade MB adsorbed or react with surface-bound H₂O to produce hydroxyl radical species, $\cdot\text{OH}$. However, the valence band level of g-C₃N₄ (1.57 eV) is not sufficient for direct oxidation of H₂O (2.27 eV) molecules through oxidation process [22]. Therefore, the photogenerated holes in g-C₃N₄ and some photogenerated holes in TiO₂ transferred from the VB of TiO₂ (+2.91 V vs. SHE) to the VB of g-C₃N₄ (+1.57 V vs. SHE) could directly degrade the MB.

As a result, the photocatalytic activity of TiO₂/g-C₃N₄ hybrid is much higher than that of pure g-C₃N₄ or TiO₂. However, with the content of TiO₂ in TiO₂/g-C₃N₄ being in excess, numerous photo-induced electrons and holes would recombine easily on the surface of TiO₂. Therefore, 40 %TiO₂/g-C₃N₄ sample exhibited the best photocatalytic activity among these different TiO₂/g-C₃N₄ photocatalysts. The result of photocurrent measurement suggests that 40 %TiO₂/g-C₃N₄ composite holds stronger ability in separation of electron–hole pairs than other samples, which is in good agreement with the mechanism suggested above.

Additionally, the thinner nanosheet structure of TiO₂/g-C₃N₄ is benefit to suppressing recombination of electrons and holes. Since the structure of each thinner nanosheet determines that the distance of the photogenerated electrons and holes move from the bulk to the particle surface is much shorter than the spherical particles done, thus the photogenerated electrons and holes can transport to the TiO₂ surface in a short time. Also, bulk recombination is reduced and the electrons and holes can be applied for photocatalytic degradation of MB efficiently.

Conclusions

In summary, we have successfully prepared the nanosheet TiO₂/g-C₃N₄ composites by a facile solvothermal method. It was found that the nanosheets TiO₂ was covered on the surface of g-C₃N₄. The influence of TiO₂ ratio on the resulting photocatalytic activity of TiO₂/g-C₃N₄ nanosheets has been investigated in detail by photocatalytic

degradation of methylene blue under visible light irradiation. It was found that TiO₂/g-C₃N₄ with 40 wt% TiO₂ exhibited the best photocatalytic activity toward photocatalytic degradation of MB, about 7 times and 10 times higher than that of g-C₃N₄ and TiO₂, respectively. The significantly improved photocatalytic activity of the nanocomposite is mainly due to the nanosheets' structure and superior electron transport property. This work demonstrates that TiO₂/g-C₃N₄ nanosheets is a very promising candidate for the development of high-performance photocatalysts with high visible-light photocatalytic activity that could find potential applications in water treatment and dye sensitized solar cells.

Acknowledgments This work has been supported by China Postdoctoral Science Foundation (2013M542415); National Nature Science Foundation of China (41305112); Youth Foundation of Xinjiang Uygur Autonomous Region (2013211B37); the "Cross-Cooperation Program for Creative Research Teams" of Chinese Academy of Sciences, and "Western Light" Program of Chinese Academy of Sciences (XBBS201126); Research projects of Education Department in Xinjiang Uygur Autonomous Region (XJEDU2011156).

References

1. X.C. Wang, K. Maeda, A. Thomas, K. Takanebe, G. Xin, J.M. Carlsson, K. Domen, M. Antonietti, *Nat. Mater.* **76**, 8 (2009)
2. X. Wang, K. Maeda, X. Chen, K. Takanebe, K. Domen, Y. Hou, X. Fu, M. Antonietti, *J. Am. Chem. Soc.* **1680**, 131 (2009)
3. S.B. Yang, Y.J. Gong, J.S. Zhang, L. Zhan, L.L. Ma, Z.Y. Fang, R. Vajtai, X.C. Wang, P.M. Ajayan, *Adv. Mater.* **2452**, 25 (2013)
4. Y. Zheng, J. Liu, J. Liang, M. Jaroniec, S.Z. Qiao, *Energy Environ. Sci.* **6717**, 5 (2012)
5. S.C. Yan, Z.S. Li, Z.G. Zou, *Langmuir* **10397**, 25 (2009)
6. M. Zhang, J. Xu, R. Zong, Y. Zhu, *Appl. Catal. B* **229**, 147 (2014)
7. L. Ge, C.C. Han, J. Liu, Y.F. Li, *Appl. Catal. A* **215**, 409–410 (2011)
8. G. Liu, P. Niu, C.H. Sun, S.C. Smith, Z.G. Chen, G.Q. Lu, H.M. Cheng, *J. Am. Chem. Soc.* **11642**, 132 (2010)
9. Y.J. Zhang, T. Mori, J.H. Ye, M. Antonietti, *J. Am. Chem. Soc.* **6294**, 132 (2010)
10. Y. Wang, Y. Di, M. Antonietti, H.R. Li, X.F. Chen, X.C. Wang, *Chem. Mater.* **5119**, 22 (2010)
11. Y.B. Wang, J.D. Hong, W. Zhang, R. Xu, *Catal. Sci. Technol.* **1703**, 3 (2013)
12. S.C. Yan, S.B. Lv, Z.S. Li, Z.G. Zou, *Dalton Trans.* **1488**, 39 (2010)
13. L. Ge, C.C. Han, J. Liu, *Appl. Catal. B Environ.* **100**, 108–109 (2011)
14. J. Sun, J. Song, M.A. Gondal, S. Shi, Z. Lu, Q. Xu, X. Chang, D. Xiang, K. Shen, *Res. Chem. Intermed.* (2014). doi:10.1007/s11164-014-1789-0
15. Y.J. Wang, R. Shi, J. Lin, Y.F. Zhu, *Energy Environ. Sci.* **2922**, 4 (2011)
16. S. Chu, Y. Wang, Y. Guo, J.Y. Feng, C.C. Wang, W.J. Luo, X.X. Fan, Z.G. Zou, *ACS Catal.* **912**, 3 (2013)
17. F. Goettmann, A. Fischer, M. Antonietti, A. Thomas, *Angew. Chem. Int. Ed.* **4467**, 45 (2006)
18. Y.J. Zhang, A. Thomas, M. Antonietti, X.C. Wang, *J. Am. Chem. Soc.* **50**, 131 (2009)
19. Y.W. Zhang, J.H. Liu, G. Wu, W. Chen, *Nanoscale* **5300**, 4 (2012)
20. X. Zhou, F. Peng, H. Wang, H. Yu, Y. Fang, *Appl. Catal. B Environ.* **718**, 142–143 (2013)
21. L. Gu, J.Y. Wang, Z.J. Zou, X.J. Han, *J. Hazard. Mater.* **216**, 268 (2014)
22. H.J. Yan, H.X. Yang, *J. Alloys Compd.* **26**, 509 (2011)
23. X. Wang, W.Y. Yang, F.T. Li, Y.B. Xue, R.H. Liu, Y.J. Hao, *Ind. Eng. Chem. Res.* **17140**, 52 (2013)
24. Z. Huang, Q. Sun, K. Lv, Z. Zhang, M. Li, B. Li, *Appl. Catal. B Environ.* **420**, 164 (2015)
25. J. Lei, Y. Chen, L. Wang, Y. Liu, J. Zhang, *J. Mater. Sci.* **3467**, 50 (2015)
26. J.G. Yu, S.H. Wang, J.X. Low, W. Xiao, *Phys. Chem. Chem. Phys.* **16883**, 15 (2013)
27. J. Lei, Y. Chen, F. Shen, L. Wang, Y. Liu, J. Zhang, *J. Alloys Compd.* **328**, 631 (2015)
28. C. Miranda, H. Mansilla, J. Yáñez, S. Obregón, G. Colón, *J. Photochem. Photobiol. A* **16**, 253 (2013)
29. H. Li, L. Zhou, L. Wang, Y. Liu, J. Lei, J. Zhang, *Phys. Chem. Chem. Phys.* **17406**, 17 (2015)

30. J. Chen, S. Qin, Y. Liu, F. Xin, X. Yin, *Res. Chem. Intermed.* **637**, 40 (2014)
31. Y. You, Z. Jiang, Y. Zhang, C. Ge, R. Li, *Res. Chem. Intermed.* **3079**, 41 (2015)
32. K. Zhao, Z. Wu, R. Tang, Y. Jiang, Y. Lu, *Res. Chem. Intermed.* **4405**, 41 (2015)
33. S.W. Bian, Z. Ma, W.G. Song, *J. Phys. Chem. C* **8668**, 113 (2009)
34. L. An, G. Wang, Y. Cheng, L. Zhao, F. Gao, Y. Tian, *Res. Chem. Intermed.* (2014). doi:[10.1007/s11164-014-1836-x](https://doi.org/10.1007/s11164-014-1836-x)
35. A. Eshaghi, S. Hayeripour, A. Eshaghi, *Res. Chem. Intermed.* (2015). doi:[10.1007/s11164-015-2161-8](https://doi.org/10.1007/s11164-015-2161-8)
36. F. Dong, L. Wu, Y. Sun, M. Fu, Z. Wu, S.C. Lee, *J. Mater. Chem.* **15171**, 21 (2011)
37. J. Yu, H. Yu, B. Cheng, X. Zhao, J. Yu, W. Ho, *J. Phys. Chem. B* **13871**, 107 (2003)
38. W. Wang, Y. Ni, C. Lu, Z. Xu, *Mater. Lett.* **161**, 111 (2013)
39. C. Han, Y. Wang, Y. Lei, B. Wang, N. Wu, Q. Shi, Q. Li, *Nano Res.* **1199**, 8 (2015)
40. Z. Liu, X. Chen, Y. Wang, Q. Tao, *Res. Chem. Intermed.* **1683**, 41 (2015)
41. K. Sridharan, E. Jang, T.J. Park, *Appl. Catal. B Environ.* **718**, 142–143 (2013)
42. K. Nagaveni, M.S. Hegde, N. Ravishankar, G.N. Subbanna, G. Madras, *Langmuir* **2900**, 20 (2004)
43. M. Kong, Y.Z. Li, X. Chen, T.T. Tian, P.F. Fang, F. Zheng, X.J. Zhao, *J. Am. Chem. Soc.* **16414**, 133 (2011)
44. X. Lü, J. Shen, D. Fan, J. Wang, Z. Cui, J. Xie, *Res. Chem. Intermed.* (2015). doi:[10.1007/s11164-015-1953-1](https://doi.org/10.1007/s11164-015-1953-1)
45. K. Dai, L. Lu, C. Liang, Q. Liu, G. Zhu, *Appl. Catal. B Environ.* **331**, 156–157 (2014)
46. A. Fujishima, T.N. Rao, D.A. Tryk, *J. Photochem. Photobiol. C* **1**, 1 (2000)